Article

Thermal Estimation and Thermal Design for Coupling Coils of 6.6 kW Wireless Electric Vehicle Charging System

Jinhai Jiang [ID], Yu Lan *, Ziming Zhang, Xingjian Zhou and Kai Song *[ID]

School of Electrical Engineering and Automation, Harbin Institute of Technology, Harbin 150001, China
* Correspondence: 21b906022@stu.hit.edu.cn (Y.L.); kaisong@hit.edu.cn (K.S.); Tel.: +86-137-6683-2633 (K.S.)

Abstract: Wireless electric vehicle charging technology is developing in the direction of high power levels. However, more generated heat brought by higher power will accelerate the system's aging and can even lead to damage. An excellent thermal design for the magnetic coupler can reduce each part's maximum temperature, ensuring long-term operation reliability. Therefore, in this article, the magnetic coupler's thermal estimation and design are studied based on a 6.6 kW wireless electric vehicle charging system. First, the calculation method of internal resistance of a litz coil, core loss, and eddy current loss of a shielding aluminum plate are studied. Considering the influence of thermal fields on material properties, each part's power loss calculation formula is further modified to improve the accuracy. After that, heat dissipation research is carried out. The heat dissipation measures, such as filling the surface of the shielding aluminum plate with thermal conductive silicone grease, are proposed. Finally, the effectiveness of the heat dissipation measures is verified by simulation and experiments. The experiment shows that the error between the power loss value of each part calculated by simulation and measured by the experiment is less than 15%, and the maximum temperature of the magnetic coupler is controlled below 80 °C.

1. Introduction

Wireless charging technology has become a research hotspot. With the developments of recent years, wireless charging technology has been widely used in electric vehicles, ships, and implantable medical devices [1]. Nowadays, wireless charging technology is developing in the direction of higher power levels [2–5]. However, a large amount of generated heat in a high-power system will accelerate the system's aging and even lead to damage due to a high system temperature [6]. Therefore, the thermal design for the high-power wireless electronic vehicle charging system is necessary. It makes it essential to establish the finite element thermal field simulation model of the magnetic coupler, accurately calculate the loss value of each part, and obtain the temperature value and temperature distribution. The losses of the magnetic coupler include litz coil loss, ferrite core loss, and shielding aluminum plate loss.

In terms of coil loss calculation, the key is to accurately calculate the internal resistance value of the litz coil when working. The traditional methods include the Biot–Savart law method [7], the improved Dowell method [8], and the Kelvin function method [9]. In addition, ref. [10] analyzed the difference between the skin effect and the proximity effect of the twisted and binding wires. Then, the equivalent internal resistance of the two coils is calculated according to the improved Dowell method. Ref. [11] analyzed the distribution characteristics of the magnetic field on the litz wire under the condition of a high-frequency excitation current and investigated the influence of the twisting degree on the internal resistance of the litz wire. However, the above methods are only applicable to a simple coil structure. The magnetic coupler in the wireless charging system further comprises the

magnetic core and aluminum plate. Their influence on the coil's internal resistance cannot be ignored.

In terms of core loss, ref. [12] studied the influence of magnetic leakage. The fitted magnetic density distribution function was substituted into the improved Steinmetz formula. Then, the core loss can be calculated. In [13], the magnetic density distribution of the magnetic core under sinusoidal excitation is studied, and the distribution law is function fitted. The magnetic density after fitting is brought into the Steinmetz formula for calculation. In 2022, ref. [14] found that when the excitation waveform contains a zero voltage interval, there is still loss on the magnetic core. Therefore, the dielectric loss on the magnetic core is simulated based on the relaxation coefficient function. However, the above methods do not consider the influence of temperature change on material loss characteristics, resulting in inaccurate calculation results.

In terms of loss measurements, ref. [15] proposed the method based on step resonance excitation but it only applies to an environment with a constant temperature. Combined with the excitation current's characteristics, ref. [16] established the thermal radiation model of the coil. The experiment proved that the loss calculation error of the established thermal radiation model was less than 25%.

As for the thermal design of wireless charging systems, ref. [17] designed a planar transformer for electric vehicle chargers. The transformer winding is placed on the outer layer of the PCB, and the contact area between winding and air is increased, improving the heat transfer coefficient between the winding and the air and suppressing the maximum temperature of the winding.

Considering the current research results, existing research is insufficient. The following problems emerge:

I　The loss analysis and calculation method of shielding aluminum plates have not been researched enough.

II　The existing loss calculation methods of wireless charging systems only apply under specific conditions, resulting in different loss calculation formulas under different working conditions. Therefore, it is necessary to establish loss models and obtain calculation methods suitable for most cases.

III　In engineering, the thermal design of the magnetic coupler is often based on experience from the heat transfer perspective. Few studies and an unclear basis cannot effectively guide design. Simulating the magnetic coupler's thermal field according to the heat transfer principle and carrying out thermal design is necessary.

2. Loss Analysis and Calculation of Magnetic Coupler

In this article, the loss values of the litz coil, ferrite core, and shielding aluminum plate in the magnetic coupler are calculated. The calculation process and method are shown in Figure 1.
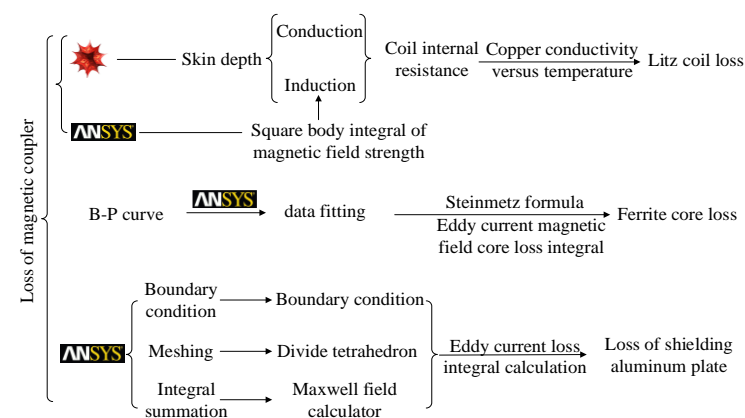

Figure 1. Loss calculation formula of each part in the magnetic coupler.

2.1. Loss Analysis of Litz Coil

The working frequency of the wireless charging system for electric vehicles is 85 kHz. Under this frequency, the equivalent internal resistance of the copper coil wound by ordinary solid core copper wire increases due to the skin effect and the proximity effect, resulting in an increased loss. The schematic diagram of the skin effect and the proximity effect of solid core copper wire is shown in Figure 2.
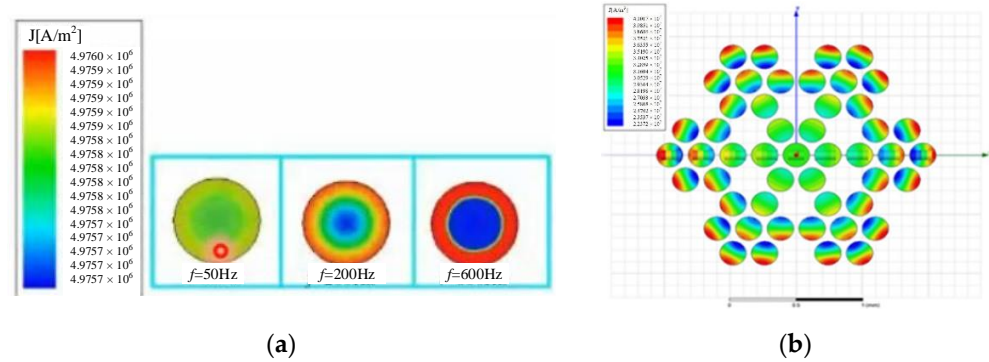

Figure 2. Schematic diagram of solid copper wire's skin effect and proximity effect. (**a**) Skin effect; (**b**) proximity effect.

For the litz wire, the power loss caused by the eddy current magnetic field is proportional to the square of the magnetic field strength. Therefore, the loss of the litz wire can be calculated based on the magnetic field strength distribution. The magnetic field distribution of the square solenoid and the magnetic field intensity distribution of litz wire can be obtained by Biot–Savart's law. The schematic diagram of the single-layer square solenoid coil is shown in Figure 3a. The loss of the coil includes conduction loss and induction loss, which correspond to conduction internal resistance R_{cond} and induction internal resistance R_{indu}. The conduction loss is related to the skin effect and internal resistance when not working. In comparison, the induction loss is related to the proximity effect caused by the eddy current magnetic field.

$$R_0 = R_{\text{cond}} + R_{\text{indu}} \tag{1}$$

Figure 3. Schematic diagram of single layer square solenoid coil. (**a**) Real solenoid coil; (**b**) simplified solenoid coil model.

The formula for induced internal resistance is shown in Formula (2).

$$R_{\text{indu}} = \frac{-4n_0 \pi \gamma \Phi_{\text{indu}}(\gamma)}{\sigma} \int_\Gamma H^2(\text{s})\text{ds} \tag{2}$$

where n_0 is the number of coil turns, and $H^2(s)$ is the square of the magnetic field strength at the longitudinal position, s, under the excitation current of 1A. σ is the conductivity of coil material. γ and $\Phi_{\text{indu}}(\gamma)$ can be calculated by (3) and (4):

$$\gamma = r_s \sqrt{\mu_0 \mu_r \sigma \omega} \tag{3}$$

$$\Phi_{\text{indu}}(\gamma) = \frac{ber(\gamma)bei'(\gamma) - bei(\gamma)ber'(\gamma)}{ber'^2(\gamma) + bei'^2(\gamma)} \tag{4}$$

where *ber*, *bei*, *bei′*, and *ber′* are Kelvin functions, and r_s is the radius of a single strand of litz wire (m).

It can be seen from Formula (4) that the square of the magnetic field strength can be calculated by the curve area. The litz wire's diameter is 0.05 mm. It is calculated that the skin depth is 0.22 mm, which is larger than the wire diameter of the litz wire. Therefore, the current flows evenly through the cross-section of the stranded wire. Equations (2) and (4) can be simplified into Equations (5) and (6):

$$R_{\text{indu}} = \frac{-4n_0 \pi \gamma \Phi_{\text{indu}}(\gamma)}{\sigma} \int_V H^2(x, y, z) \mathrm{d}v \tag{5}$$

$$\Phi_{\text{indu}}(\gamma) = -\frac{\gamma^3}{16} \tag{6}$$

where *I* is the excitation current of the litz wire (A), *S* is the cross-sectional area of the coil (m²), and $\int_V H^2(x, y, z) dv$ is the volume fraction of the square of the magnetic field strength.

The internal conduction resistance of the litz wire can be calculated by the Formula (7):

$$R_{\text{cond}} = \sum_{i=1}^{N} \left(\frac{2\pi r_i}{\pi r_s^2 n_0 \sigma} \right) = \sum_{i=1}^{N} \frac{2r_i}{r_s^2 n_0 \sigma} \tag{7}$$

where *N* is the turn number of the litz coil.

The calculation formula of equivalent internal resistance and coil loss can be obtained from Formulas (5)–(7):

$$R_0 = \frac{n_0 \pi \gamma^4}{4I^2 S \sigma} \int_V H^2(x, y, z) \mathrm{d}v + \sum_{i=1}^{N} \frac{2r_i}{r_s^2 n_0 \sigma} \tag{8}$$

$$P_{\text{Litz}} = I^2 R_0 \tag{9}$$

The volume fraction of the square of the magnetic field strength in Equation (8) can be solved by the field calculator in the finite element software Maxwell.

The system's temperature will rise when working, resulting in changes in material parameters. For litz coil, its interior is mainly composed of copper. When the temperature increases, it can be seen from Formula (8) that the conductivity of copper decreases. Figure 4 shows the change curve of copper resistivity with temperature. It shows that the resistivity of copper with temperature can be approximated as a first-order function between 0–100 °C. The relationship can be substituted into Formula (8) to obtain the litz coil loss calculation formula considering the temperature effect, as shown in Formula (10).

$$\begin{cases} R_0 = \frac{1}{\sigma_{\text{Cu}}(t)} \left[\frac{n_0 \pi \gamma^4}{4I^2 S} \int_V H^2(x, y, z) \mathrm{d}v + \sum\limits_{i=1}^{N} \frac{2r_i}{r_s^2 n_0} \right] \\ \sigma_{\text{Cu}}(t) = (-0.02438t + 6.32) \times 10^7 \end{cases} \tag{10}$$

where $\sigma_{\text{Cu}}(t)$ is the function of copper conductivity with temperature, and *t* is the temperature (°C).
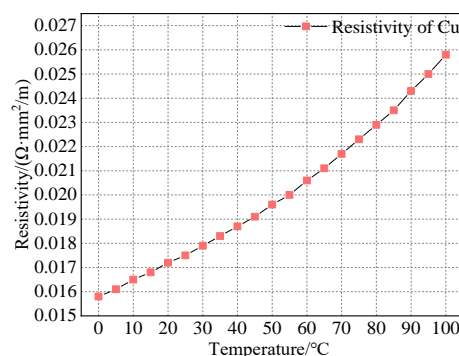

Figure 4. Change curve of copper resistivity with temperature.

2.2. Loss Analysis of Magnetic Core

The loss of the ferrite core P_{core} consists of three parts, the hysteresis loss P_{h}, the eddy current loss P_{e}, and the residual loss P_{ex}. The hysteresis loss can be expressed by the hysteresis loop, as shown in Figure 5. The area enclosed by the curve in the figure is the hysteresis loss, which is finally dissipated in the form of heat.
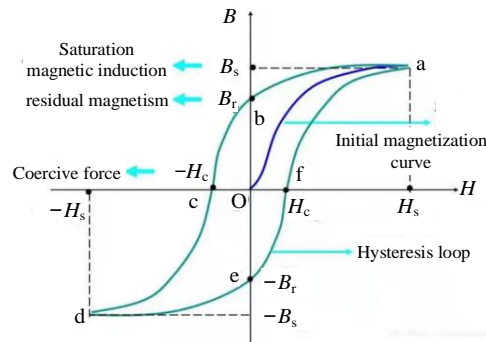

Figure 5. Hysteresis loop.

Combined with the Bertotti loss separation method, the expression of core loss P_{core} is obtained, as shown in the Formula (11).

$$P_{\text{core}} = P_{\text{h}} + P_{\text{e}} + P_{\text{ex}} = k_{\text{h}} f B_{\text{m}}^{x} + k_{\text{e}} f^2 B_{\text{m}}^2 + k_{\text{ex}} f^{1.5} B_{\text{m}}^{1.5} \tag{11}$$

where k_{h}, k_{e}, and k_{ex} are the hysteresis loss coefficient, the eddy current loss coefficient, and the residual loss coefficient. B_{m} is the peak magnetic induction intensity (T), f is the excitation current frequency (Hz), and x is the Steinmetz coefficient corresponding to hysteresis loss.

The hysteresis loss and eddy current loss of the magnetic core can be calculated by Formula (12) in engineering:

$$P_{\text{core}} = C_{\text{m}} f^{\alpha} B_{\text{m}}^{\beta} \tag{12}$$

Equation (12) is the Steinmetz formula. C_{m}, α, and β is the Steinmetz coefficient obtained by fitting the loss value under sinusoidal ac excitation at different frequencies. In general, the value range of α is 1 to 2, and the value range of β is 2 to 3. The core loss can be calculated by inputting the B-P curve values under different frequencies into ANSYS Maxwell according to the material properties, as shown in Figure 6.
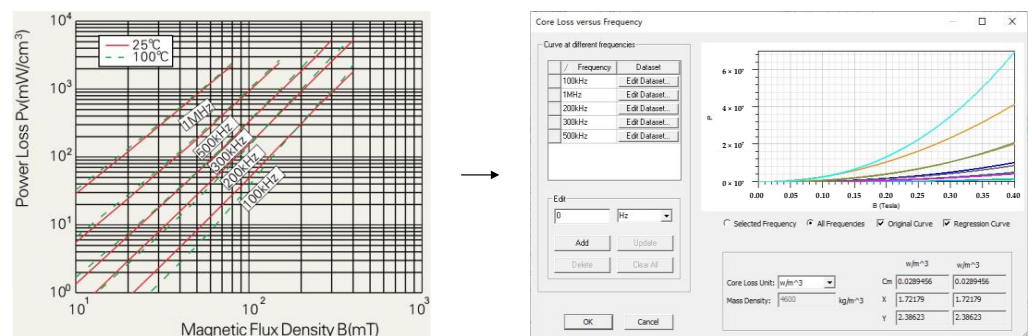

Figure 6. B-P curve data fitting of magnetic ferrite core.

Similarly, the temperature rise will also affect the loss of the ferrite core. According to the loss versus temperature curve, the change of the core loss with temperature can be approximated into a quadratic function. Based on the quadratic function relationship obtained by fitting, the core loss formula is modified by modifying the Steinmetz coefficient, as shown in Formula (13).

$$P_{\text{core}} = C_{\text{m}} \times (0.000068t^2 - 0.01t + 1.195) \times f^{\alpha} B_{\text{m}}^{\beta} \tag{13}$$

2.3. Loss Analysis and Calculation of Shielding Aluminum Plate

In the wireless charging system, the shielding aluminum plate can generate a magnetic field opposite to the coil through the eddy current effect, preventing the radiated electromagnetic energy from exceeding the limit value. Figure 7 compares the spatial magnetic induction intensity of the magnetic coupler with the shielding aluminum plate and without it.

(**a**)　　　　　　　　　　　　　　　　　　　　　　(**b**)
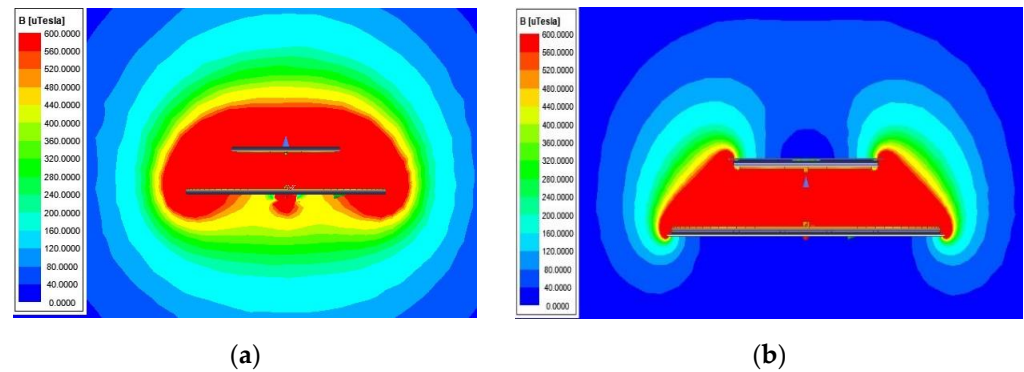
Figure 7. Cloud diagram of the magnetic induction intensity distribution in the magnetic coupler under different conditions. (**a**) Magnetic induction intensity distribution without aluminum plate; (**b**) magnetic induction intensity distribution with aluminum plate.

The loss on the shielding aluminum plate is mainly the eddy current loss. Considering the skin effect, the eddy current loss of the aluminum plate can be expressed as:

$$\mathrm{d}P_{\mathrm{Al}} = \frac{E^2}{R_{\mathrm{Al}}} \tag{14}$$

$$E = \frac{L^2 \mathrm{d}B}{\mathrm{d}t} \tag{15}$$

$$R_{\mathrm{Al}} = \frac{4L}{\sigma \delta \mathrm{d}L} \tag{16}$$

where P_{Al} is the loss of the aluminum plate, E is the potential on the aluminum plate, and R_{Al} is the equivalent resistance of the aluminum plate unit.

Combined with (15) and (16), the calculation formula for the eddy current loss of the unit aluminum plate can be obtained.

$$\mathrm{d}P_{\mathrm{Al}} = \frac{\sigma L^3 \delta \mathrm{d}L}{4} \left(\frac{\mathrm{d}B}{\mathrm{d}t}\right)^2 \tag{17}$$

For the calculation of the eddy current loss of the whole aluminum plate, it is necessary to integrate the Formula (17) from 0 to L/2. Integrating the calculation result from 0 to T, the calculation formula of the aluminum plate loss can be obtained.

$$P_{\mathrm{Al}} = \frac{hf^2}{16\sigma\pi^2\mu^2} \int_0^T \left(\frac{\mathrm{d}B}{\mathrm{d}t}\right)^2 \mathrm{d}t \tag{18}$$

where ρ is the material resistivity ($\Omega \cdot$m), h is the aluminum plate thickness (m), and B is the magnetic induction strength (T). d is the metal body material thickness (m), f is the excitation current frequency (Hz), and ρ is the material density (kg/m^3). The upper and lower surfaces of the aluminum plate are square, the side length is l, the thickness is h, and the skin depth is δ. The length of the unit aluminum plate is dL, as shown in Figure 8.
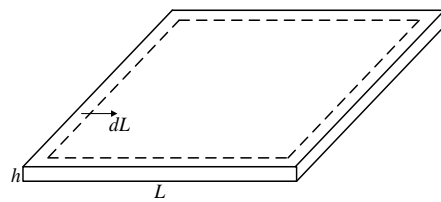
Figure 8. Schematic diagram of a geometric model of shielding aluminum plate.

According to (18), it can be concluded that the eddy current loss of the aluminum plate gradually increases with the decrease in its conductivity σ. The aluminum plate loss of different aluminum plate conductivities is shown in Figure 9.
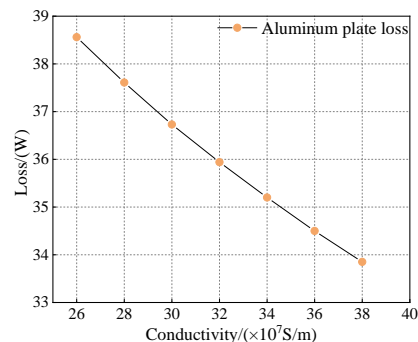
Figure 9. Variation of aluminum plate loss with aluminum plate conductivity.

The finite element analysis method can be introduced to calculate the aluminum plate loss. Figure 10 shows that the aluminum plate loss is mainly concentrated at the edge of the aluminum plate and is relatively small in the middle area. The mesh division is shown in Figure 11. It shows that the aluminum plate has a large number of units at the edge, which corresponds to the loss distribution of the aluminum plate. After division, the eddy current loss of each aluminum plate division block is calculated and integrated to obtain the complete aluminum plate loss.
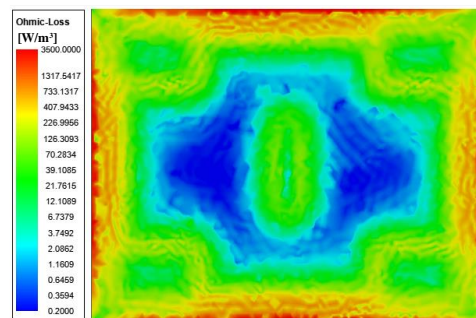

**Figure 10.** Loss distribution diagram of the aluminum plate in simulation results.

The resistivity of aluminum increases with the increase in temperature. According to (18), it can be concluded that the loss of the aluminum plate will increase. The change of aluminum versus temperature change is shown in Figure 12, similar to the curve of resistivity of copper versus temperature. It can be approximated into a first-order function, and the expression can be substituted into (18) to obtain the loss calculation formula for shielding aluminum plates.

$$\begin{cases} P_{\text{Al}} = \frac{hf^2}{16\sigma_{\text{Al}}(t)\pi^2\mu^2} \int_0^T \left(\frac{\mathrm{d}B}{\mathrm{d}t}\right)^2 \mathrm{d}t \\ \sigma_{\text{Al}}(t) = (-0.01578t + 4.086) \times 10^7 \end{cases} \tag{19}$$

where $\sigma_{\text{Al}}(t)$ is the function of aluminum conductivity with temperature.
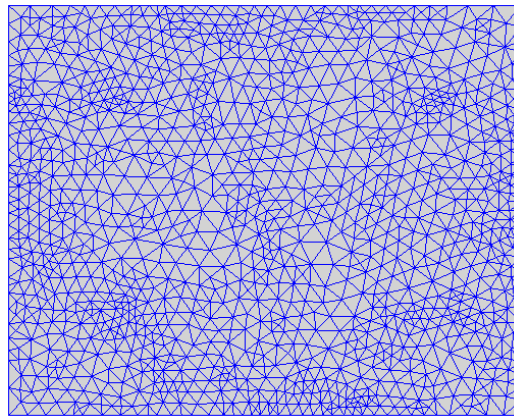
Figure 11. Grid division of aluminum plate.
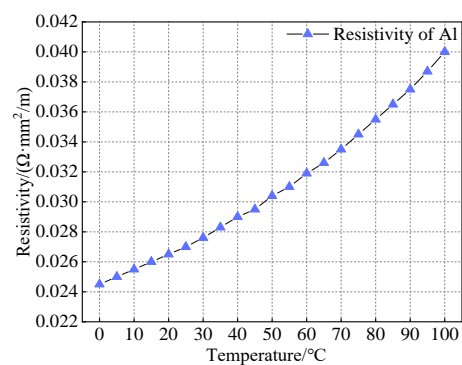
**Figure 12.** Variation curve of aluminum resistivity with temperature.

3. Thermal Simulation and Heat Dissipation Research

3.1. Thermal Simulation and Analysis of the Magnetic Coupler

In the process of temperature rise, due to the effects of three heat transfer modes: heat conduction, heat convection, and heat radiation, the temperature of each part of the magnetic coupler tends to be stable, reaching a thermal equilibrium state. The schematic diagram of the heat transfer mode is shown in Figure 13.
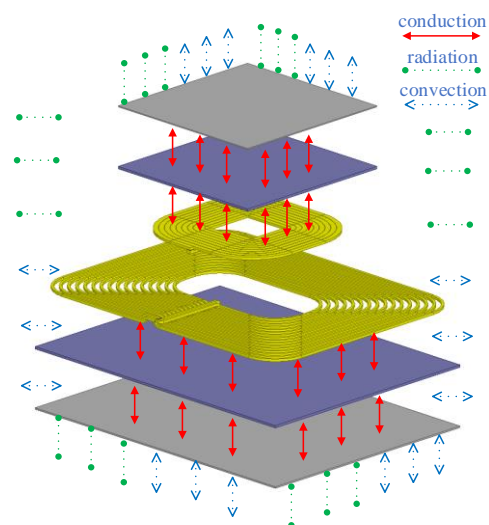
Figure 13. Schematic diagram of heat transfer mode of the magnetic coupler.

There is a heat conduction process between each part of the magnetic coupler of the wireless charging system. The support parts and cover plates do not generate heat, and

their temperature rise comes from the heat conduction process of the litz coil, ferrite core, and shielding aluminum plate. The heat generated by the litz coil and the ferrite core is radiated out through the shielding aluminum plate on the surface of the magnetic coupler. The heat transfer capacity between the air and the shielding aluminum plate depends on the convective heat transfer coefficient. Generally, under the natural convection condition of the air environment, the convective heat transfer coefficient is 5–25 W/(m^2·K). Under the forced convection condition of the gas, the convective heat transfer coefficient can be increased to 300 W/(m^2·K). The above three heat exchange processes makes it so that the temperature of the magnetic coupler can not increase indefinitely. However, if the temperature distribution is not uniform, the material parameters in the high-temperature area will change. Then, the heat generated is greater than the heat lost under the original heat balance condition, resulting in the continuous rise of the system temperature and eventual damage.

In order to evaluate the heat generation of the magnetic coupler, it is necessary to conduct a thermal field simulation. First, under the eddy current magnetic field, the loss model of the magnetic coupler can be established, and the loss value of each part can be calculated. The electromagnetic material parameters of each part are shown in Table 1. The main thermal field material parameters of each part required for thermal field simulation are shown in Table 2.

Table 1. Electromagnetic field material parameters of the magnetic coupler's coil, core, and aluminum plate.
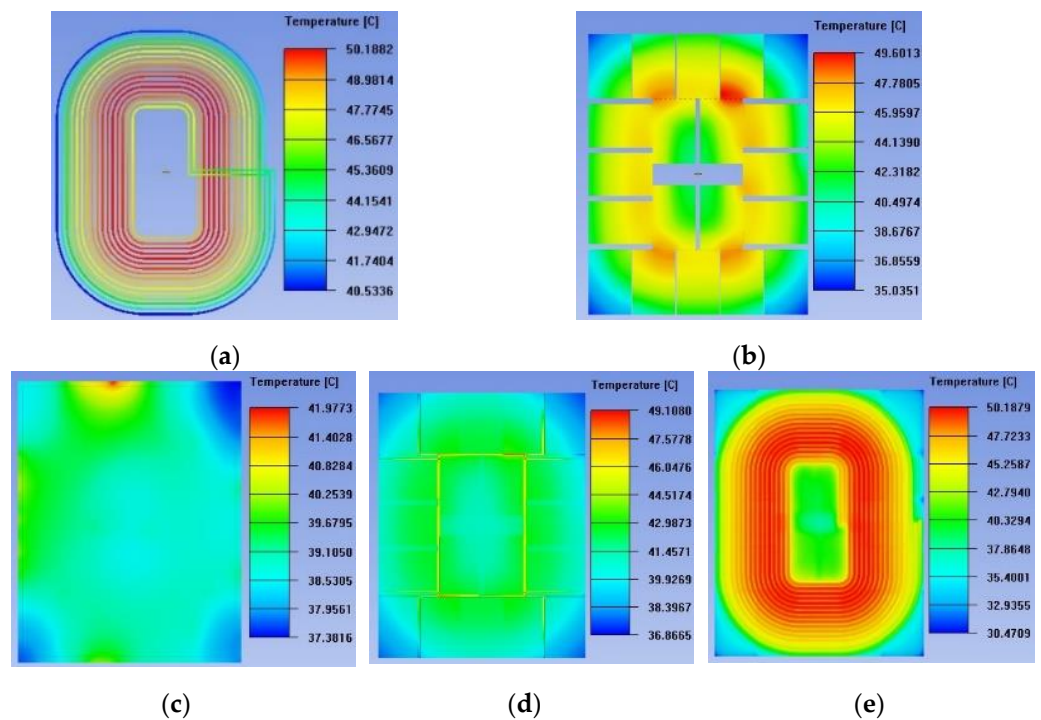
Category	Coil	Magnetic Core	Aluminum Plate
Conductivity (S/m)	58,000,000	1.00	38,000,000
Relative permeability	0.99	3300	1.00
Relative dielectric constant	1.00	12	1.00

Table 2. Thermal field material parameters of the magnetic coupler's coil, core, and aluminum plate.
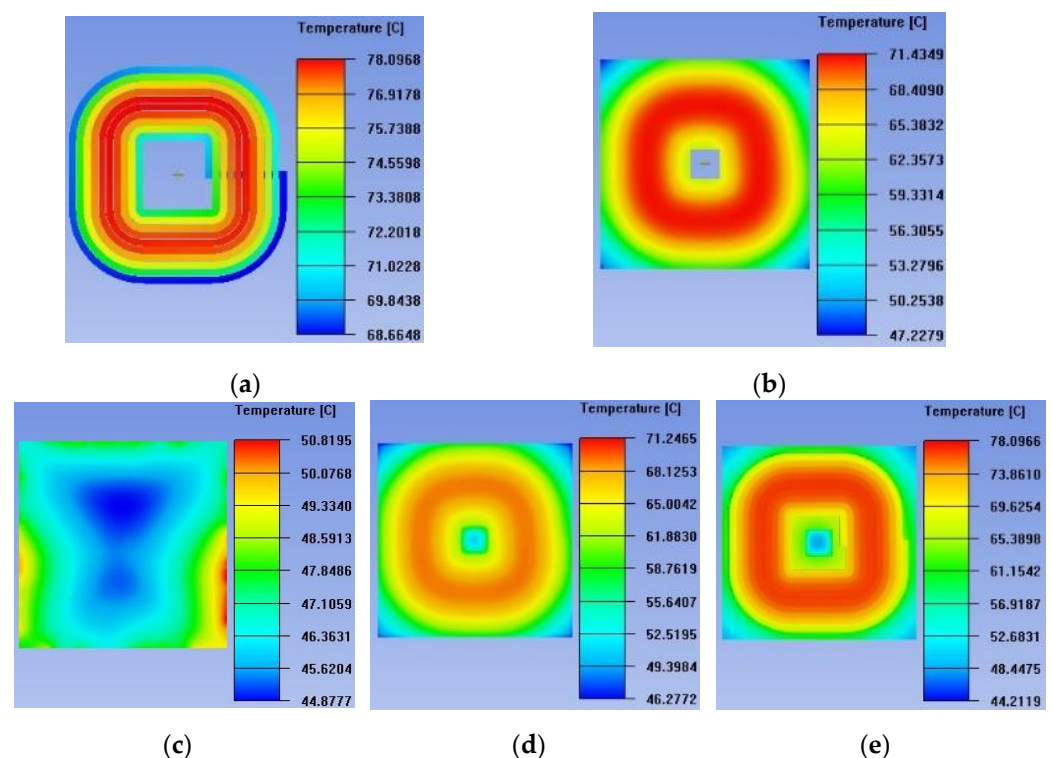
Category	Coil	Magnetic Core	Aluminum Plate
Specific heat capacity (J/(kg·K))	390	750	880
Density (kg/m^3)	8933	4600	2700
Thermal conductivity (W/m·K)	387.6	4	240

Eddy current magnetic field and thermal field simulations are conducted for the magnetic coupler of a 6.6 kW electric vehicle wireless charging system. A thermal field simulation for the magnetic coupler's heat generation is shown in Figures 14 and 15. The simulation results are presented in the form of temperature distribution. (a), (b), and (c) show the coil, the magnetic core, and the aluminum plate temperatures. In addition, the magnetic coupler's mechanical structure includes a coil tray and a cover plate. They have no electrical properties and do not generate heat. Their temperature distributions are shown in (c) and (d).

According to Figures 14 and 15, the temperature of each part of the secondary magnetic coupler is higher than that of the primary side coupler. The highest temperature is in the middle of the secondary litz coil, with a temperature range of 68.7–78.1 °C. The temperature distribution is high in the middle area and low on the inner and outer sides. It is because the litz wire on the outer side can dissipate heat outward, and that on the inner side can dissipate heat through the internal opening. The wire in the middle part is difficult to dissipate heat outward, resulting in higher temperatures. The temperature distribution of the ferrite core is similar to that of the coil. However, the temperature distribution on the shielding aluminum plate is related to its loss distribution. According to the previous analysis, the loss of the aluminum plate is mainly concentrated at the edge, resulting in a low surface center temperature and a high surrounding temperature.

Figure 14. The temperature of each part of the primary magnetic coupler. (**a**) Primary coil; (**b**) primary magnetic core; (**c**) primary aluminum plate; (**d**) primary cover plate; and (**e**) primary wire tray.


Figure 15. The temperature of each part of the secondary magnetic coupler. (**a**) Secondary coil; (**b**) secondary magnetic core; (**c**) secondary aluminum plate; (**d**) secondary cover plate; and (**e**) secondary wire tray.

While the magnetic coupler is working, the litz wire tray and cover plate do not generate power loss. The litz coil, the ferrite core, and the aluminum plate transfer heat to the litz wire tray and the cover plate by heat conduction, making the litz wire tray and the

cover plate generate a temperature rise. According to Figures 14e and 15e, the temperature distribution of the litz wire tray can reflect the outline of the litz coil, and the maximum temperature of the wire tray is basically the same as the maximum temperature of the litz coil. The temperature distribution of the cover plate is affected by the magnetic core and the aluminum plate, where the temperature in the middle region is lower than that in the edge region.

3.2. Heat Dissipation Research of the Magnetic Coupler

The magnetic coupler's thermal design steps are shown in Figure 16. First, the geometric model of the magnetic coupler is established. Then, the material properties are determined in the magnetic field, the boundary conditions are set, and the mesh is divided. The losses of each part of the coupler are obtained based on the eddy current magnetic field control equation. After that, the loss is brought into the thermal field. The thermal field's material properties are determined, the boundary conditions are set, and the mesh is divided. The temperature of each part of the magnetic coupler is obtained based on the governing equation of the thermal field. Finally, loop iteration until convergence. This section will research different heat dissipation methods based on this process.
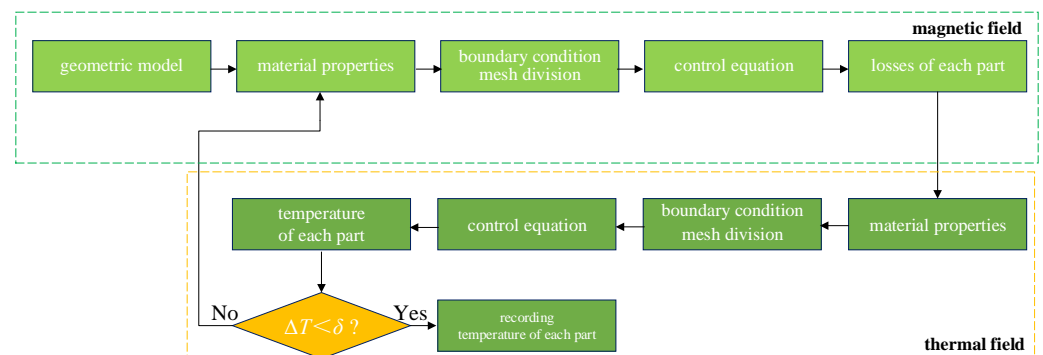

Figure 16. The magnetic coupler's thermal design steps.

In addition to the litz coil, ferrite core, and shielding aluminum plate, the magnetic coupler includes the wire tray and cover plate. They play a supporting and fixing role, called supporting materials. The difference in thermal conductivity of different support materials caused different heat dissipated from the litz coil and ferrite core. As a result, the final thermal equilibrium temperature is different. In this section, the influence of four supporting materials is studied. The parameters of four supporting materials are shown in Table 3, and the simulation results are shown in Figure 17.

Table 3. Parameters of supporting materials.

| Category	Polystyrene	Teflon	FR4	Bakelite
Thermal conductivity (W/m·K)	0.14	0.24	0.35	0.50
Emissivity	0.86	0.86	0.90	0.90

According to Table 3 and Figure 17, when the material's emissivity is approximately equal, the maximum temperature gradually decreases with the increase in the thermal conductivity λ of the support material. For the secondary coil, the maximum temperature difference is nearly 5 °C with different support materials. Therefore, selecting a material with a high thermal conductivity as the supporting material can reduce the maximum temperature of each part of the magnetic coupler to a certain extent.
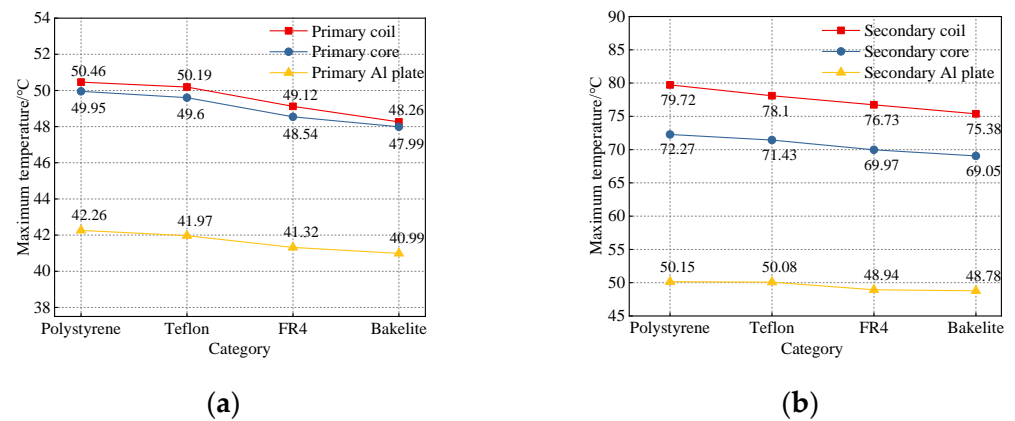
Figure 17. Variation of the maximum temperature of each part of the magnetic coupler with supporting material. (**a**) Primary magnetic coupler; (**b**) secondary magnetic coupler.

The heat generated by the litz coil and ferrite core is dissipated to the outside through the aluminum plate. Strengthening the heat dissipation ability of the aluminum plate can reduce the maximum temperature. According to the thermal radiation formula $\phi = \varepsilon A \sigma_0 \left(T_1^4 - T_2^4 \right)$, when the heat dissipation area of the aluminum plate is fixed, the larger the surface emissivity ε, the more the heat is radiated outward ϕ. Therefore, improving the emissivity of the aluminum plate can strengthen its heat dissipation ability. The surface emissivity of a smooth aluminum plate is 0.04, the oxidized aluminum plate can reach 0.4, and the aluminum plate coated with heat dissipation silicone grease is approximately 0.9.

As seen in Figure 18, the maximum temperature of each part decreases with the increased emissivity of the aluminum plate surface. For the litz coil of the secondary magnetic coupler, the temperature changes by nearly 3 °C.
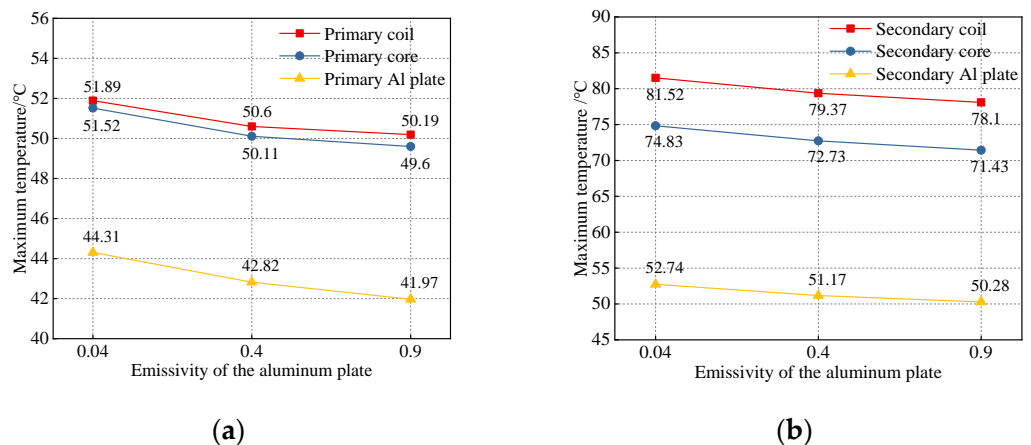
Figure 18. Variation of the maximum temperature of each part of the magnetic coupler with emissivity of the aluminum plate. (**a**) Primary magnetic coupler; (**b**) secondary magnetic coupler.

4. Experimental Verification

In order to verify the accuracy of the loss calculation and the effectiveness of the heat dissipation scheme, a 6.6 kw electric vehicle wireless charging experimental platform is built. The physical diagram of the experimental platform is shown in Figure 19. The experimental platform includes power factor correction (PFC), a primary inverter, compensation topology, a magnetic coupler, a secondary rectifier, an electronic load, and control operation equipment.
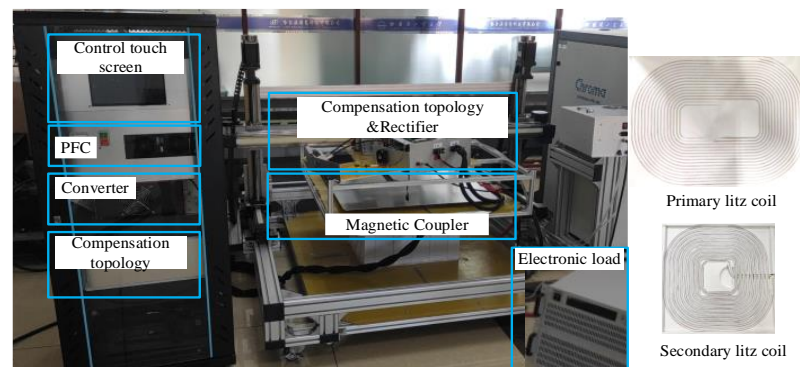
Figure 19. A 6.6 kw electric vehicle wireless charging system experimental platform.

4.1. Loss Measurement of the Magnetic Coupler

The litz coil used in the magnetic coupler in this article is made of 4200 litz wires with a diameter of 0.05 mm, which are wound in a double winding mode. The magnetic core is DMR95 ferrite, and its saturated magnetic induction strength B_S exceeds 500 mT. Therefore, under the working condition of the 6.6 kW system, it is unnecessary to consider the influence of magnetic saturation on the system efficiency. The shielding aluminum plate is made of 6061 aluminum, which has a good performance on corrosion resistance and oxidation effect. The supporting material is a Bakelite plate, which can be used continuously at 260 °C and meets the safety requirements of the experiment. The main parameters of each part of the magnetic coupler are shown in Table 4.

Table 4. Main parameters of each part of the magnetic coupler.

Parameter	Primary Side	Secondary Side
Coil winding form	Double strand parallel winding for 8 turns	Double strand parallel winding for 10 turns
Turn spacing	6.5 mm	1 mm
Wire width	180 mm	109 mm
Wire diameter	5 mm	5 mm
Core size	650 mm × 510 mm	350 mm × 350 mm
Core thickness	5 mm	5 mm
Aluminum plate size	675 mm × 535 mm	375 mm × 375 mm
Aluminum plate thickness	3 mm	2 mm

Under a transmission distance of 140 mm, the loss simulation and experimental results of each part of the magnetic coupler are shown in Table 5. The loss proportion is shown in Figure 20.

Table 5. Loss of each part of the magnetic coupler.

| Category	Simulated Loss Value (W)	Experimental Loss Value (W)
Primary coil	58.23	51.00
Primary core	78.80	79.21
Primary aluminum plate	38.81	
Secondary coil	50.59	
Secondary core	9.74	115.31
Secondary aluminum plate	13.50	

(a)

(b)
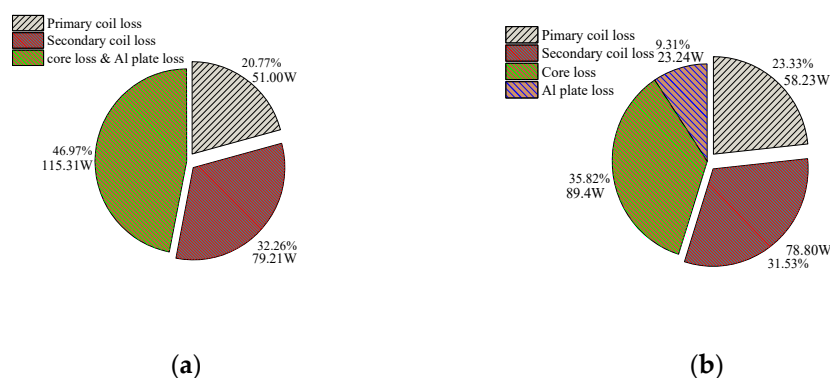
Figure 20. Loss ratio of simulation and experiment. (**a**) Loss ratio of the experiment; (**b**) loss ratio of simulation.

Table 5 and Figure 20 show that the loss values of each part of the magnetic coupler obtained by simulation are almost consistent with the experiment, with an error of 15%.

4.2. Temperature Experimental Verification of the Magnetic Coupler

The accuracy of the simulation results can be determined by obtaining the temperature distribution of each part of the magnetic coupler. The Yokogawa PG10 temperature recorder and thermocouple sensors are used to measure the temperature value. Before the experiment, the thermocouple sensors were embedded in the areas with higher temperatures, as shown in Figure 21. However, the thermocouple will be disturbed due to the high-frequency and strong magnetic field environment. Therefore, the temperature rise curve of each part of the magnetic coupler cannot be obtained. The following temperature test process is adopted to solve this problem.


(a)

(b)

(c)

(d)

(e)

(f)
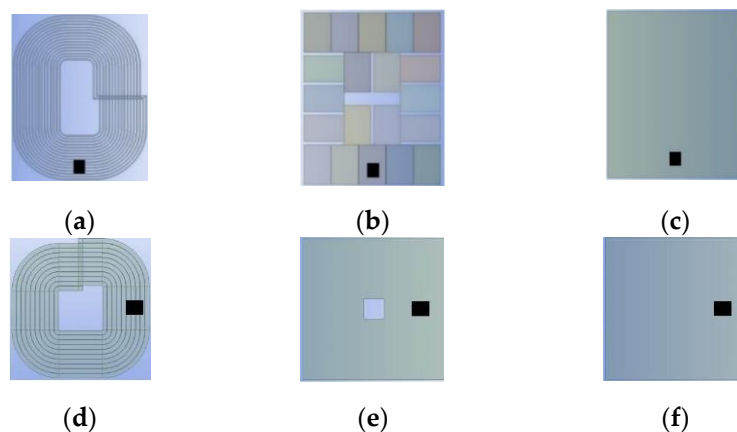
Figure 21. Embedded position of thermocouple sensors. (**a**) Primary coil; (**b**) primary magnetic core; (**c**) primary aluminum plate; (**d**) secondary coil; (**e**) secondary magnetic core; and (**f**) secondary aluminum plate.

First, start the temperature recorder and obtain the initial temperature value of each part through the embedded thermocouple sensor. Second, power on the system. The infrared thermal imager can be used to measure the temperature of the secondary side shielding aluminum plate. When the surface temperature of the secondary side shielding aluminum plate has no obvious change, the system can be powered off. Finally, continue to record the temperature value when powering off. The temperature will suddenly change at this time, and the abrupt temperature value can be regarded as the actual temperature of each part of the magnetic coupler. The temperature of the secondary side shielding aluminum plate after powering off is shown in Figure 22, and the temperature curve in the temperature recorder is shown in Figure 23.

(a)

(b)

Figure 22. The temperature of the secondary shielding aluminum plate of the magnetic coupler. (**a**) The shielding aluminum plate; (**b**) the temperature value and distribution of the shielding aluminum plate.


(a)

(b)
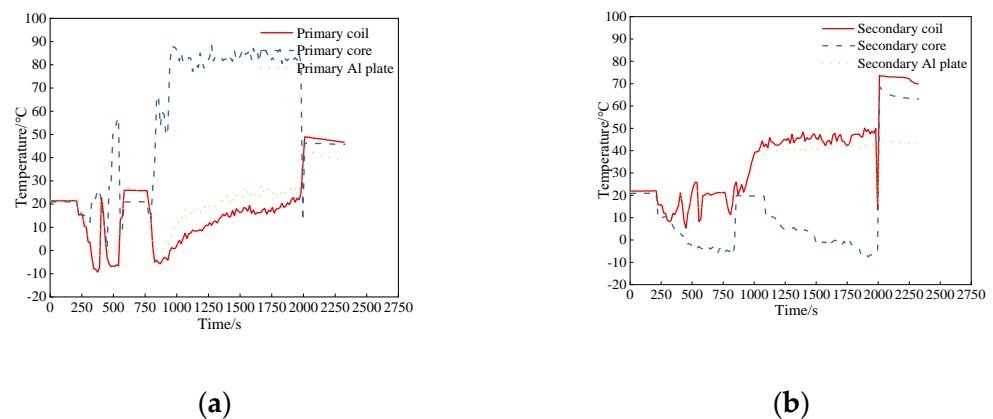
Figure 23. Temperature curve of each part of the magnetic coupler. (**a**) Temperature curve of each part of the primary side; (**b**) temperature curve of each part of the secondary side.

Table 6 compares the temperature obtained by thermal field simulation with the experiment. It shows that the temperature values obtained by simulation and experiment are in good agreement.

Table 6. Temperature of each part of the magnetic coupler.

Value	Simulated Temperature (°C)	Experimental Temperature (°C)
Primary coil	49.69	48.9
Primary core	43.68	46.2
Primary aluminum plate	40.01	44.1
Secondary coil	76.79	73.6
Secondary core	70.66	68.7
Secondary aluminum plate	45.98	42.8

After that, thermal conductive silicone grease is applied to the secondary shielding aluminum plate. Figure 24 shows the temperature of the secondary shielding aluminum plate after working for a while. Compared with Figure 22, it can be seen that applying thermal conductive silicone grease reduces the temperature value of the secondary shielding aluminum plate to a certain extent and makes the temperature distribution more uniform.

<center>(a)   (b)</center>
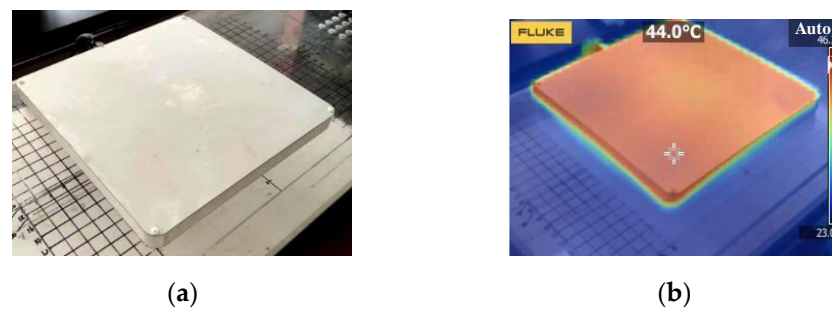
Figure 24. The temperature of secondary shielding aluminum plate coated with thermal conductive silicone grease. (**a**) Shielding aluminum plate coated with thermal conductive silicone grease; (**b**) temperature value and distribution.

The main reasons for the difference between the temperature values obtained by the simulation and the experiment are as follows:

I   Due to the heat conduction process between the parts of the magnetic coupler, the temperature of the thermocouple sensor rises, resulting in an error in the actual measured temperature value.

II   When processing the experimental data, the temperature after powering off is taken as the temperature of each part of the magnetic coupler, resulting in an error.

III   The simulation model is based on finite element mesh division. Considering the simulation accuracy and time, the convergence condition of the model is set to an error of less than 1%. It will also lead to a little difference between simulation and experimental results.

5. Conclusions

In this article, the loss types of a litz coil, ferrite core, and shielding aluminum plate in a magnetic coupler are analyzed at first. Then, the calculation formula for the internal resistance of the litz coil is obtained by the Kelvin function method, and the loss of the ferrite core is calculated by the Steinmetz formula. Based on the skin depth, the calculation formula of the eddy current loss of a shielding aluminum plate is derived. In addition, the influence of temperature change on the loss of each part is considered. Next, the improved loss calculation formula for each part of the magnetic coupler is obtained by curve fitting. The accuracy of the loss calculation of the magnetic coupler is verified by measuring the internal resistance and efficiency. The error between the simulated and measured values is less than 15%. After that, the thermal equilibrium temperature of each part is obtained by thermal field simulation, and the temperature distribution is analyzed. Finally, in terms of the magnetic coupler's heat generation, the effects of the types of internal support materials and aluminum plate heat dissipation on the temperature are studied. The experimental results show that the filling of thermal conductive silicone grease on the surface of the shielding aluminum plate is conducive to the heat dissipation of the magnetic coupler.

Author Contributions: Theoretical analysis, K.S.; simulation, X.Z.; experiment, Z.Z.; writing—original draft preparation, Y.L.; writing—review and editing, J.J. All authors have read and agreed to the published version of the manuscript.

Conflicts of Interest: The authors declare no conflict of interest.

References

1. Zhang, Z.; Pang, H.; Georgiadis, A.; Cecati, C. Wireless power transfer-an overview. *IEEE Trans. Ind. Electron.* **2019**, *66*, 1044–1058. [CrossRef]
2. Minnaert, B.; Stevens, N. Maximizing the power transfer for a mixed inductive and capacitive wireless power transfer system. In Proceedings of the 2018 IEEE Wireless Power Transfer Conference (WPTC), Montreal, QC, Canada, 3–7 June 2018.
3. Yeo, T.D.; Kwon, D.; Khang, S.T.; Yu, J.W. Design of maximum efficiency tracking control scheme for closed-loop wireless power charging system employing series resonant tank. *IEEE Trans. Power Electron.* **2016**, *32*, 471–478. [CrossRef]
4. Pries, J.; Galigekere, V.P.N.; Onar, O.C.; Su, G.J. A 50-kw three-phase wireless power transfer system using bipolar windings and series resonant networks for rotating magnetic fields. *IEEE Trans. Power Electron.* **2020**, *35*, 4500–4517. [CrossRef]
5. Zhang, Y.; Yan, Z.; Liang, Z.; Li, S.; Mi, C.C. A high-power wireless charging system using lcl-n topology to achieve a compact and low-cost receiver. *IEEE Trans. Power Electron.* **2019**, *35*, 131–137. [CrossRef]
6. Ashok, B.; Kannan, C.; Mason, B.; Ashok, S.D.; Indragandhi, V.; Patel, D.; Wagh, A.S.; Jain, A.; Kavitha, C. Towards safer and smarter design for lithium-ion-battery-powered electric vehicles: A comprehensive review on control strategy architecture of battery management system. *Energies* **2022**, *15*, 4227. [CrossRef]
7. Deng, Q.; Liu, J.; Czarkowski, D.; Kazimierczuk, M.K.; Bojarski, M.; Zhou, H.; Hu, W. Frequency-dependent resistance of litz-wire square solenoid coils and quality factor optimization for wireless power transfer. *IEEE Trans. Ind. Electron.* **2016**, *63*, 2825–2837. [CrossRef]
8. Wojda, R.; Kazimierczuk, M.K. Winding resistance and power loss of inductors with litz and solid-round wires. *IEEE Trans. Ind. Appl.* **2018**, *54*, 3548–3557. [CrossRef]
9. Liu, J.; Deng, Q.; Czarkowski, D.; Kazimierczuk, M.K.; Zhou, H.; Hu, W. Frequency optimization for inductive power transfer based on ac resistance evaluation in litz-wire coil. *IEEE Trans. Power Electron.* **2019**, *34*, 2355–2363. [CrossRef]
10. Wang, S.; Dorrell, D.G. Copper loss analysis of ev charging coupler. *IEEE Trans. Magn.* **2015**, *51*, 1–4. [CrossRef]
11. Chen, B.; Tao, X.; Wan, N.; Fang, C.; Tang, B. Analysis and calculation of high frequency loss characteristics of incompletely twisted litz wire. *High Volt. Eng. China* **2022**, 1–12.
12. Chen, Y.; Zhang, H.; Shin, C.S.; Jo, C.H.; Park, S.J.; Kim, D.H. An efficiency optimization-based asymmetric tuning method of double-sided lcc compensated wpt system for electric vehicles. *IEEE Trans. Power Electron.* **2020**, *35*, 11475–11487. [CrossRef]
13. Liu, B.; Chen, W.; Wang, J.; Chen, Q. A practical inductor loss testing scheme and device with high frequency pulsewidth modulation excitations. *IEEE Trans. Ind. Electron.* **2021**, *68*, 4457–4467. [CrossRef]
14. Zhou, Y.; Xie, W.; Ma, C.; Huang, L. Modeling core losses under exciting waveforms with zero voltage period in power converters. *IEEE Trans. Ind. Electron.* **2022**. *accepted*. [CrossRef]
15. Kalra, G.R.; Pearce, M.G.; Kim, S.; Thrimawithana, D.J.; Covic, G.A. A power loss measurement technique for inductive power transfer magnetic couplers. *IEEE J. Emerg. Sel. Topics Ind. Electron.* **2020**, *1*, 113–122. [CrossRef]
16. Alsayegh, M.; Saifo, M.; Clemens, M.; Schmuelling, B. Magnetic and thermal coupled field analysis of wireless charging systems for electric vehicles. *IEEE Trans. Magn.* **2019**, *55*, 1–4. [CrossRef]
17. Zhang, Z.; Liu, C.; Wang, M.; Si, Y.; Liu, Y.; Lei, Q. High-efficiency high-power-density cllc resonant converter with low-stray-capacitance and well-heat-dissipated planar transformer for ev on-board charger. *IEEE Trans. Power Electron.* **2020**, *35*, 10831–10851. [CrossRef]